Pressureless sintering of LRH nanoplates on amorphous alumina for near-infrared GAP: Mn^{4+} transparent ceramic film

Jing Yao[a], Lu Chen[a], Qi Zhu[a*], Ji-Guang Li[b]

[a]*Key Laboratory for Anisotropy and Texture of Materials (Ministry of Education), School of Materials Science and Engineering, Northeastern University, Shenyang, Liaoning 110819, China*

[b]*Research Center for Functional Materials, National Institute for Materials Science, Namiki 1-1, Tsukuba, Ibaraki 305-0044, Japan*

*Corresponding author

Dr. Qi Zhu

Tel: +86-24-8367-2700

E-mail: zhuq@smm.neu.edu.cn

Abstract

Transparent ceramics have become a research hotspot in the preparation of fluorescent materials in recent years because of their excellent physical and chemical properties and high transparency. Gadolinium aluminate, as a stable matrix material, is often doped with various active ions to obtain luminescence with different colors. However, it is very difficult to fabricate gadolinium aluminate transparent ceramics by a traditional method, although they are the charming solid lighting materials. Here, we developed a pressureless sintering method to prepare $GdAlO_3$: Mn (GAP: Mn) transparent ceramic films, which were prepared by spin coating rare earth hydroxide (LRH) on amorphous alumina substrate and sintering at 1550 ^oC for 2 hours. Through the interface reaction, the Al_2O_3 reacts with Gd_2O_3 to form mesophase $Gd_4Al_2O_9$ below 1550 ^oC. However, the final products are $GdAlO_3$ at 1550 ^oC. The GAP: Mn^{4+} film exhibits a high transmittance of over 90%. Under UV excitation at 310 nm, the ceramic film outputs deep red and NIR emissions, which are both arising from the ^2E_g-$^4A_{2g}$ transition of Mn^{4+}. Due to the electron traps arising from unequal valence substitution, the ceramic film exhibits a negative thermal quenching phenomenon. The ceramic film has a good luminescence thermal stability, because its emission intensity at 150 ^oC maintains over 72% that at room temperature. This work may pave a new way to fabricate transparent ceramics using rare earth hydroxides.

Keywords*:* Transparent ceramics; $GdAlO_3$; Mn^{4+}; Interface reaction; Layered rare earth hydroxide

1. Introduction

The perovskite family of materials has attracted extensive attention due to the various interesting properties such as ferroelectricity, photoluminescence, superconductivity, and magnetoresistance [1, 2]. Perovskite ($CaTiO_3$) was first discovered by Gustav Rose in 1839 and named after the Russian mineralogist L.A. perovskite [3]. In recent years, a lot of researches have been done on the luminescence of solid perovskites, including luminescence in powders, single crystals, thin films, and amorphous materials. Metal halogenated perovskite materials have a wide range of applications in the fields of solar cells, photodetectors and light-emitting diodes [4, 5, 6]. The most representative oxide perovskite material is $CaTiO_3$. In 1997, Diallo et al. [7] reported the Pr^{3+} doped calcium titanate material for the first time, and they discussed and analyzed the red luminescence and the spectral properties of $CaTiO_3$: Pr^{3+} phosphors in detail. After that, $CaTiO_3$: Pr^{3+} materials were given a lot of research [8, 9, 10], and the ion types doped with $CaTiO_3$ gradually increased, including Dy^{3+} doped white phosphors [11], Eu^{3+} doped red phosphors [12], Bi^{3+} doped yellow phosphors [13] and Sm^{3+} doped orange-red phosphors [14], etc. Due to the special structure of perovskite oxide (ABO_3), many types of ions can substitute for A or B site, resulting in perovskite luminescent materials. Because of their stable structure and excellent optical properties, they have great research significance and value in the fields of light, electricity and magnetism. According to the investigation, most perovskite rare earth fluorescent materials are mainly concentrated in the three systems of $GdAlO_3$, $LaAlO_3$ and $YAlO_3$, while the electrons in the 4*f* sublayer of Gd^{3+} are half filled, the 4*f* electrons of La^{3+} are fully filled, while Y^{3+} has no 4*f* electrons [15]. Therefore, they are relatively stable as matrix materials, and can be incorporated into the body by different activators to obtain different types of luminescence.

In recent years, there are abundant studies and reports on different types of $YAlO_3$ and $LaAlO_3$ as matrix materials, while there are relatively few studies on $GdAlO_3$ as matrix materials. In 1995, Dorenbos et al. [16] reported the scintillation characteristics of $GdAlO_3$ single crystals doped with different concentrations of Ce^{3+} grown by horizontal directional crystallization technology. In 1999, Jovanic et al. [17]

reported Cr^{3+} doped $GdAlO_3$, which was expected to be a good pressure sensor. At that time, there were many researches on $GdAlO_3$ matrix, while there were relatively few rare earth ion doped materials. In 2014, Wang et al. [18] reported the hydrothermal synthesis of $GdAlO_3$: Eu^{3+} microcrystals and discussed the effect of reaction temperature on the formation of $GdAlO_3$ and the fluorescence characteristics of $GdAlO_3$: Eu^{3+}. Shilpa et al. [19] synthesized $GdAlO_3$: Eu^{3+}, Bi^{3+} nano phosphors by solution combustion technology. The addition of Bi^{3+} makes the emission of phosphors change from orange red to dark red, which is expected to be used as the red component in WLED. Up to now, the activated ions used by $GdAlO_3$ as matrix materials are mainly Eu^{3+} [19, 20] and Ce^{3+} [16, 17, 18, 19, 20, 21], and a small number include Yb^{3+} (yellow), Tb^{3+} (blue and green), Pr^{3+} (blue and red), Er^{3+} (green), Cr^{3+} and Mn^{4+} (near infrared). Moreover, most of the studies are carried out to characterize the fluorescence properties by making $GdAlO_3$ nanocrystals or phosphors, and there are few reports on $GdAlO_3$ transparent ceramics.

The unit cell structure of $GdAlO_3$ (GAP) is a tetrahedron (a=5.305 Å, b=7.448 Å, c=5.254 Å), which belongs to orthogonal ABO_3 perovskite structure. $GdAlO_3$ is a distorted perovskite. Gd^{3+} changes from 12 to 8 coordination with oxygen atoms in the ideal perovskite, and Al^{3+} still maintains 6 coordination with oxygen atoms. Its space group is *Pbnm,* which deviates from the cubic space group *Pm*3*m* due to the distortion of $[BO_6]$ octahedron. The $[AlO_6]$ octahedral cluster is arranged along the c crystal axis, and the $[GdO_8]$ polyhedron is connected with the $[AlO_6]$ octahedron in a collinear or coplanar manner [22]. This special structure makes it possible optimize or realize the tunable luminescence characteristics through a variety of doping or composition modification.

Fluorescent materials are usually prepared in the form of powders or transparent ceramics. Due to its excellent physical and chemical properties, high transmittance and easy preparation into various shapes, transparent ceramics have better performance in the fields of high-power and high-density devices, as well as light-emitting devices that have special requirements for their appearance and need to be integrally molded. It is more and more favored by modern society at present.

Transparent ceramics can be widely found in solid-state lasers, transparent armor, scintillators, optical components, and solid-state lighting [23, 24, 25, 26, 27, 28].

Manganese, a non-rare earth element with multiple oxidation states, is considered a promising alternative to europium or chromium for the design of red to near-infrared sustained-emitting phosphors. In recent years, Mn^{4+}-activated phosphors have received extensive research and attention [29, 30, 31, 32, 33]. Compared with rare earth ions, it is cheaper, and Mn^{4+} is greatly affected by the crystal field and will emit a strong deep red or near-infrared according to the crystal field. Mn^{4+}-doped phosphors have been used in the lighting industry as a red component, usually exhibiting broadband excitation and sharp red emission. On the other hand, Mn^{4+} can emit near-infrared light, which also has potential application prospects in biomedical imaging and other fields [34]. The emission of manganese mainly depends on its valence state, ion distribution and local coordination environment. The Mn^{4+} ions with the $3d^3$ electronic configuration can be stably located in an octahedral symmetric environment, and their optical properties are strongly influenced by the local environment and the covalency of the Mn-ligand bond [34, 35]. The electron-phonon coupling and covalency of Mn^{4+} ligand bonds could lead to strong or weak crystal field, which depends on the host lattice and can realize the desired tunable luminescence. Due to the feasible substitution between Al^{3+} (0.535 Å, CN=6) and Mn^{4+} (0.53 Å, CN=6) ions, gadolinium aluminate ($GdAlO_3$) with perovskite crystal structure is a suitable host for Mn^{4+} doping.

In this work, a novel strategy was proposed for the growth of $GdAlO_3$: Mn^{4+} (GAP: Mn^{4+}) transparent ceramic films on the amorphous alumina substrate by an interfacial reaction. Characterization of the films was achieved by XRD, FT-IR, SEM, UV-Vis-NIR, PLE/PL spectroscopy, temperature-dependent PL spectroscopy, and luminescence decay analysis. The ceramic film outputs deep red and NIR emissions and exhibits a negative thermal quenching behavior. The transparent film with a high transmittance has a good luminescence thermal stability. The outcomes may broaden the application of rare earth hydroxide and play a demonstration role on other transparent ceramics.

2. Experimental section

2.1 Synthesis

The starting material for rare earth source is Gd_2O_3 (99.99% pure, Huizhou Ruier Rare-Chem. Hi-Tech. Co. Ltd, Huizhou, China) and the starting material for manganese source is $Mn(NO_3)_2$ (50 wt%). Manganese nitrate, ammonia hydroxide (NH_4OH, 25 wt%), nitric acid (HNO_3, 67 wt%) and anhydrous ethanol (C_2H_5OH, 99.7%) were purchased from Sinopharm Chemical Reagent Co. Ltd. The aqueous solution of $Gd(NO_3)_3$ was made by dissolving the powder of Gd_2O_3 in nitric acid.

Synthesis of LRH and LRH: Mn crystals. In a typical synthesis, a mixed aqueous solution containing 2 mmol of $Gd(NO_3)_3$ and $Mn(NO_3)_2$ (Gd: Mn molar ratio of 99.1:0.9) was prepared under magnetic stirring at room temperature. After titrated with NH_4OH solution, the pH value of colloidal suspension was adjusted to ~7. Then the white suspension was transferred to a Teflon lined stainless-steel autoclave of 100 mL capacity for hydrothermal reaction. The final product was collected *via* centrifugation, followed by washing with deionized water (three times) and anhydrous ethanol (one time). Gd-based LRH in absence of Mn was prepared in the same way.

Fabrication of GAP transparent ceramic film. The LRH crystals were put on a transparent amorphous alumina substrate by spin coating, followed by calcined at 800 ^oC, 1000 ^oC, 1300 ^oC and 1550 ^oC for 2 h, respectively. $GdAlO_3$ (GAP) transparent ceramic films directly growed on the amorphous alumina substrate through an interfacial reaction.

2.2 Characterization

X-ray diffractometry (XRD, Model SmartLab, Rigaku, Tokyo, Japan) was used for phase identification under 40 kV/40 mA, using nickel filtered Cu-Kα radiation (λ = 0.15406 nm) with a scanning speed of 6.0^o/2θ per minute and scanning range of 5^o-60^o. Fourier transform infrared spectroscopy (FT-IR, Model Nicolet iS5, Thermo Fisher Scientific, Madison, WI, USA) was conducted by the standard KBr method. Field emission scanning electron microscopy (FE-SEM, Model JSM-7001F, JEOL, Tokyo) was used to analyze the morphology and microstructure of the products under an acceleration voltage of 15 kV. At room temperature, photoluminescence were

analyzed by a fluorescence spectrophotometer (Model FP-8600, JASCO, Tokyo) equipped with a 150 W Xe-lamp as the excitation source and an integrating sphere (Model ISF-513, JASCO, Tokyo). UV-vis-NIR spectrophotometer (UV-3600 plus, Shimadzu, Kyoto, Japan) was used to analyze the transmittance of the samples at room temperature.

3. Results and discussion

3.1 Synthesis and characterization of LRH and LRH: Mn crystals

Based on our previous research, LRH crystals were synthesized by a hydrothermal reaction [36, 37, 38]. Figure 1a shows the XRD patterns of LRH and LRH: Mn. The hydrothermal products are layered rare-earth hydroxides in a pure phase form, because all the diffraction peaks can well match to the reported data [36, 37, 38]. The (00*l*) diffraction peaks, such as (002) and (004), show the unique layered structure, while the appearance of (*hk*0) diffraction peak, such as (220), confirms the well-developed layered structure of the compounds. No other impurities are formed, which implies that single phases of Gd LRH and Gd/Mn binary LRH solid solution were successfully synthesized. Thus, incorporation of manganese ions has no obvious effect on the XRD diffraction peak of LRH (Figure 1a).

Figure 1b shows the FT-IR spectra of LRH and LRH: Mn. The absorption peak at the range of 3500~3750 cm^{-1} originates from the vibration of the hydroxyl (OH^-), and the absorption peaks at the range of 3000~3500 cm^{-1} and at ~1631 cm^{-1} are owing to the O-H and H-O-H stretching vibration of H_2O, respectively [39, 40]. The appearance of these vibrations directly confirms the existence of molecular water in layered rare earth hydroxides. The absorption peak at ~1358 cm^{-1} in LRH and LRH: Mn is attributed to the bending vibration of NO_3^- [39, 40]. XRD and FT-IR spectra both show that the incorporation of manganese ions has no significant effect on the structure of LRH. Figure 1c, d shows the FE-SEM images of LRH and LRH: Mn, respectively. The nanoplates in Figure 1c are hexagonal platelets of about 200 nm with smooth surface and clear edge. The crystallinity of LRH becomes worse after manganese ion doping (Figure 1d), accompanied by rough surfaces and fuzzy edges. However, the

nanoplates of LRH and LRH: Mn with two- dimensional morphology are suitable for fabrication of functional films, which may be comparable with the exfoliated nanosheets [37, 41].

3.2 Characterization and structure evolution of the ceramic film

In absence of pressure, GAP and GAP: Mn transparent ceramic films directly growed on the amorphous alumina substrate. Figure 2 is the schematic diagram of preparing GAP ceramic film, which shows the whole process of the experiment. In order to explore the formation mechanism of GAP, the prepared LRH precursor nanoplates were coated on the surface of amorphous alumina and calcined at 800 °C, 1000 °C, 1300 °C, 1550 °C for 2 hours, respectively. Figure 3 shows the XRD patterns of GAP film and GAP: Mn film at different temperatures. The XRD results indicate that only cubic structured Gd_2O_3 was preferentially formed on the substrate at 800 °C, and Al_2O_3 did not react with rare earth oxide at the interface. When the temperature is rising to 1000 °C, although the main calcined products are also Gd_2O_3, there is a small trace of $Gd_4Al_2O_9$, mainly due to that a few Al_2O_3 reacted with Gd_2O_3 at the interface to form the intermediate phase of $Gd_4Al_2O_9$ following the reaction as below:

$$Gd_2O_3 + Al_2O_3 \rightarrow Gd_4Al_2O_9 \quad (1)$$

When the temperature increased to 1300 °C, a mixture of Gd_2O_3, $Gd_4Al_2O_9$ and $GdAlO_3$ was found, indicating increased amount of Al_2O_3 reacted with Gd_2O_3 though the interfacial reaction at this temperature. Obviously, increasing the temperature yielded fewer amounts of Gd_2O_3 and increased amount of gadolinium aluminate, such as $Gd_4Al_2O_9$ and $GdAlO_3$. The alumina reacted with Gd_2O_3 and $Gd_4Al_2O_9$ to form $GdAlO_3$, which is the gadolinium aluminate with higher aluminum content. The reaction follows the equation as below:

$$Gd_2O_3 + Al_2O_3 \rightarrow Gd_4Al_2O_9 \quad (2)$$

$$Gd_4Al_2O_9 + Al_2O_3 \rightarrow GdAlO_3 \quad (3)$$

Increasing the calcination temperature up to 1550 °C only yielded $GdAlO_3$ (termed as GAP), indicating the temperature to form GAP is at higher than 1300 °C (Figure 3). The XRD pattern of GAP: Mn is consistent with GAP, both of which are pure GAP

phase, confirming that manganese ions are successfully incorporated into the GAP matrix.

Figure 4 is SEM morphology of the films calcined at various temperatures. At 800 °C, LRH like particles are found in the film (Figure 4a). Increasing the temperature to 1000 °C, the film is composed of small particles with fuzzy edges (Figure 4b). However, the film is composed of dense grains at 1300 °C, and most grains have sizes of 300-500 nm (Figure 4c). There is no observation of particles in the film. The grains grow up to 1-2 μm with increasing the temperature to 1550 °C (Figure 4d). However, the grain size of bulk ceramic fabricated through the traditional high-temperature reaction is about 10-30 μm [42, 43, 44, 45]. Because the two-dimensional morphology restricted the grain growth during the interface reaction, obviously smaller grain size is found for the ceramic films. Also due to the low temperature of 1550 °C and short reaction time of 2 hours for the interface reaction, the ceramic film has the small grain sizes, comparing with that for the bulk ceramic, which is fabricated by the traditional reaction at the high temperature of 1700 °C-1800 °C through vacuum sintering [42, 43, 44, 45].

The effect of calcination temperatures (800 °C, 1000 °C, 1550 °C) on the element distribution of Gd and Al for the films on Al_2O_3 substrate is analyzed in Figure 5. Because the main phase is Gd_2O_3 at 800 °C, Gd is found for the film along with a small trace of Al, which is arising from the Al_2O_3 substrate. Elevating the temperature resulted in the Gd content decreased from ~97.71% at 800 °C to ~72.82% at 1000 °C, and then to ~45.51% at 1550 °C. But the Al content increased from ~2.29% at 800 °C to ~27.18% at 1000 °C, and then to ~54.49% at 1550 °C. The higher the temperature is, the more Al_2O_3 participates in the interface reaction. The Al_2O_3 reacts with Gd_2O_3 to form $GdAlO_3$ at 1550 °C, but the products are Gd_2O_3 and the mesophases of $Gd_4Al_2O_9$ at the temperature lower than 1550 °C. Closely observation finds that the Al content at various temperatures is a little higher than that for the crystallization phases. For example, the Gd: Al molar ratio for $GdAlO_3$ is 1:1, but the test result is 1:1.2 for the film calcined at 1550 °C. Because the amorphous Al_2O_3 from the substrate is excess for the interface reaction, the Al content is higher than that for the target

composition.

Figure 6 shows the EDS-mapping results and FE-SEM images of the ceramic film cross section. According to the FE-SEM images, the thickness of the film is about 600-800 nm. EDS-mapping shows that the Al and Gd content change abruptly at the interface, which confirms the existence of $GdAlO_3$ film on Al_2O_3 substrate. The changed area is in good agreement with the thickness of ceramic film. The above results show that $GdAlO_3$ ceramic film with uniform distribution and reliable composition were successfully prepared through the interface reaction.

3.3 Luminescence and negative thermal quenching behavior of GAP: Mn^{4+} transparent ceramic film

Figure 7a, b shows photoluminescence excitation (PLE) and photoluminescence emission (PL) spectra of GAP: Mn^{4+} transparent ceramic film. The PLE spectrum of GAP: Mn^{4+} film monitored at 698 nm is mainly divided into a strong excitation bands (250-350 nm) centered at 310 nm and a weak excitation bands near 400 nm (Figure 7a). The broad excitation bands at 290 nm, 323 nm and 401 nm are attributed to the charge transfer band of Mn^{4+}-O^{2-}, the $^4A_{2g}$-$^4T_{1g}$ and $^4A_{2g}$-$^2T_{2g}$ transitions of Mn^{4+}, respectively [46]. Under the excitation of 310 nm ultraviolet light, the PL spectrum shows three peaks at 682 nm, 698 nm and 719 nm (Figure 7b). Due to the electron phonon coupling of Mn^{4+} in the main body, there is a partially allowed spin forbidden ^2E_g-$^4A_{2g}$ transition (698 nm) [47], and the related phonon sideband vibration of Mn^{4+} in MnO_6 octahedron. Figure 7c is the mechanism diagram of luminescence of GAP: Mn^{4+}. Under the excitation of ultraviolet light, the electrons are excited from the ground state energy level $^4A_{2g}$ to the Mn^{4+}-O^{2-} charge transfer band, and the excited state energy levels $^4T_{1g}$ and $^2T_{2g}$. Then they transfer to the ^2E_g energy level through non radiative relaxation, and finally fall back to the ground state $^4A_{2g}$, which contribute to the excellent near-infrared light output. Figure 7d shows the CIE coordinate diagram calculated from the PL spectral data of GAP: Mn^{4+}. It can be observed that the color coordinate value of the sample is (0.730, 0.270), which is located at the deep red area of the CIE diagram, which is consistent with the PL

spectrum. Because the emission peaks are at 650-750 nm, which are in visible and NIR wavelength range, the ceramic film both outputs deep red and NIR emissions. The inset in Figure 7d shows the photo of GAP: Mn^{4+} ceramic film under real-time ultraviolet excitation, confirming that the ceramic film exhibits deep red emission.

Figure 8a shows the transmittance curve of the prepared GAP: Mn^{4+} ceramic film and its appearance under daylight. There is broad and intense band at 250-400 nm in the transmittance curve, which is assigned to the absorption of Mn^{4+}-O^{2-} charge transfer, $^4A_{2g}$-$^4T_{1g}$ and $^4A_{2g}$-$^2T_{2g}$ transitions of Mn^{4+} respectively. At the visible wavelength range of 400 nm-650 nm, the ceramic film exhibits a transmittance of over 90%, while the transmittance of bare amorphous alumina substrate is about ~99.5%. Under the amorphous alumina coated with ceramic film, the words can also be clearly observed (inset in Figure 8a), further confirming that high transmittance of GAP: Mn^{4+} ceramic film. Figure 8b shows the fluorescence decay curve of GAP: Mn^{4+} ceramic film and the data of the curve could be fitted into a single exponential. The determined fluorescence lifetime of the sample is about 1.656 ms according to the following formula:

$$I = A\exp(-t/\tau) + B \quad (4)$$

where τ is fluorescence lifetime (ms), t is decay time (ms), I is fluorescence intensity, A and B are constants. Most lifetimes for Mn^{4+} activated phosphors are reported at the value range of 1.259-4.13 ms, and the calculated lifetime of the ceramic film falls in the range [48, 49, 50, 51].

In order to evaluate the luminescent performance of transparent ceramic films, temperature-dependent PL spectra ranging from 25 °C to 300 °C were analyzed in Figure 9a. The shape and the position of all peaks in the emission spectra do not significantly change with the increased temperature, but the emission intensity of the peaks decreases. The relative integral intensity of the emission peaks at various temperatures is summarized in Figure 9b. It can be observed that the fluorescence intensity of the PL peak shows a trend of increasing first and then decreasing. This negative thermal quenching effect is caused by the electron trap arising from the

unequal valence substitution between the tetravalent manganese ions and the trivalent aluminum ions. As shown in Figure 9c, the electrons are excited by ultraviolet light from the ground state energy level to the excited state energy level, and the electron traps capture the electrons from the excited state energy level through tunneling [52]. The captured electrons are released back to the excited state by heating processing, and the excited state obtains the released electrons to compensate for the loss of thermal fluorescence quenching. However, with the further increase of temperature, the captured electrons are empty, and the fluorescence intensity cannot be compensated, so the emission intensity decreases naturally. With the increase of temperature, the PL emission peak at 150 °C still maintained the fluorescence intensity more than 72% that at room temperature. The above results show that the GAP: Mn^{4+} transparent ceramic film has a good thermal stability under the excitation of 310 nm UV light.

4. Conclusion

In this work, a novel strategy for the synthesis of GAP and GAP: Mn^{4+} transparent ceramic films was reported, that is, the ceramic films could be successfully prepared by an interfacial reaction of LRH and LRH: Mn nanoplates on the amorphous alumina substrate. Characterization of the films was achieved by XRD, FT-IR, SEM, UV-Vis-NIR, PLE/PL spectroscopy, temperature-dependent PL spectroscopy, and luminescence decay analysis. Phase evolution of the film was analyzed at the temperature range from 800 °C to 1550 °C. The higher temperature makes more Al_2O_3 gradually participate in the interface reaction, and react with Gd_2O_3 to form mesophase $Gd_4Al_2O_9$, and finally to form $GdAlO_3$ at 1550 °C. Due the two-dimensional restricted grain growth, the grain size of the film is about 1-2 μm. The GAP: Mn^{4+} film exhibits a high transmittance of over 90%. Under the excitation of 310-nm ultraviolet light, GAP: Mn^{4+} film exhibits three emission peaks at 682 nm, 698 nm and 719 nm, arising from the ^2E_g-$^4A_{2g}$ transition of Mn^{4+}. Therefore, the ceramic film outputs deep red and NIR emissions. Because of unequal valence substitution between the tetravalent manganese ions and the trivalent aluminum ions,

the ceramic film exhibits a negative thermal quenching phenomenon. The emission intensity of the ceramic film at 150 °C maintains over 72% that at room temperature, indicating it has a good luminescence thermal stability.

Notes

The authors declare no competing financial interest.

Acknowledgements

This work was supported in part by the Natural Science Foundation of Liaoning Province (Grant 2020-MS-081), and National Natural Science Foundation of China (Grant 51302032, 51972047, 52172112).

References

1. C.C. Stoumpos, C.D. Malliakas, J.A. Peters, Z. Liu, M. Sebastian, et al. Crystal growth of the perovskite semiconductor $CsPbBr_3$: a new material for high-energy radiation detection. Cryst Growth Des. 2013;13:2722-2727.
2. S. Wang, Z. Liu, J.A. Peters, M. Sebastian, S.L. Nguyen, et al. Crystal growth of Tl_4CdI_6: a wide band gap semiconductor for hard radiation detection. Cryst Growth Des. 2014;14:2401-2410.
3. Z. Cheng, J. Lin. Layered organic–inorganic hybrid perovskites: structure, optical properties, film preparation, patterning and templating engineering. CrystEngComm. 2010;12:2646-2662.
4. P. Tockhorn, J. Sutter, R. Colom, L. Kegelmann, A. Al-Ashouri, et al. Improved quantum efficiency by advanced light management in nanotextured solution-processed perovskite solar cells. ACS photonics. 2020;7:2589-2600.
5. H. Wang, R. Haroldson, B. Balachandran, A. Zakhidov, S. Sohal, et al. Nanoimprinted perovskite nanograting photodetector with improved efficiency. ACS nano. 2016;10:10921-10928.
6. D. Yang, G. Zhang, R. Lai, Y. Cheng, Y. Lian, et al. Germanium-lead perovskite

light-emitting diodes. Nat Commun. 2021;12:1-7.

7. P. Diallo, P. Boutinaud, R. Mahiou, J. Cousseins. Red luminescence in Pr^{3+}-doped calcium titanates. Phys Status Solidi A. 1997;160:255-263.
8. R. Chen, F. Song, D. Chen, Y. Peng. Improvement of the luminescence properties of $CaTiO_3$: Pr obtained by modified solid-state reaction. Powder Technol. 2009;194:252-255.
9. Y. Pan, Q. Su, H. Xu, T. Chen, W. Ge, et al. Synthesis and red luminescence of Pr^{3+}-doped $CaTiO_3$ nanophosphor from polymer precursor. J Solid State Chem. 2003;174:69-73.
10. D. Wang, H. He, X. Wang, Y. Yu, L. Jiang, et al. Grain size influence on the flexibility and luminous intensity of inorganic $CaTiO_3$: Pr^{3+} crystal nanofibers. Ceram Int. 2021;47:31329-31336.
11. F. Liu, Y. Fang, N. Zhang, G. Zhao, Y. Liu. Enhancement of white light emission of Dy^{3+}: $CaTiO_3$ phosphor by Li^+ co-doping. J Mater Sci : Mater Electron. 2015;26:3933-3938.
12. B.-G. Park. Photoluminescence of Eu^{3+}-doped $CaTiO_3$ perovskites and their photocatalytic properties with a metal ion loading. Chem Phys Lett. 2019;722:44-49.
13. R. Cao, T. Fu, H. Xu, W. Luo, D. Peng, et al. Synthesis and luminescence enhancement of $CaTiO_3$: Bi^{3+} yellow phosphor by codoping Al^{3+}/B^{3+} ions. J Alloys Compd. 2016;674:51-55.
14. M.G. Ha, M.R. Byeon, T.E. Hong, J.S. Bae, Y. Kim, et al. Sm^{3+}-doped $CaTiO_3$ phosphor: synthesis, structure, and photoluminescent properties. Ceram Int. 2012;38:1365-1370.
15. B. Grabmaier. Luminescent Materials, Springer Verlag, Berlin, 1994.
16. P. Dorenbos, E. Bougrine, J. De Haas, C. Van Eijk, M. Korzhik. Scintillation properties of $GdAlO_3$: Ce crystals1. Radiat Eff Defect S. 1995;135:321-323.
17. B. Jovanić, J. Andreeta. $GdAlO_3$: Cr^{3+} as a new pressure sensor. Phys Scr. 1999;59:274.
18. X.-L. Wang, Z. Yang, J. Li, W.-F. Fu, P. Tang, et al. Hydrothermal synthesis,

morphology and luminescent properties of $GdAlO_3$: Eu^{3+} microcrystals. J Alloys Compd. 2014;614:40-43.

19. C. Shilpa, A.K. Jayaram, N. Dhananjaya, H. Nagabhushana, S. Prashantha, et al. $GdAlO_3$: Eu^{3+}: Bi^{3+} nanophosphor: synthesis and enhancement of red emission for WLEDs. Spectrochim Acta Part A: Mol. Biomol Spectrosc. 2014;133:550-558.
20. P. Jisha, R. Naik, S. Prashantha, H. Nagabhushana, S. Sharma, et al. Facile combustion synthesized orthorhombic $GdAlO_3$: Eu^{3+} nanophosphors: structural and photoluminescence properties for WLEDs. J Lumin. 2015;163:47-54.
21. C. Michail, N. Kalyvas, I. Valais, S. David, I. Seferis, et al. On the response of $GdAlO_3$: Ce powder scintillators. J Lumin. 2013;144:45-52.
22. A. Srivastava, M. Brik. The nature of Mn^{4+} luminescence in the orthorhombic perovskite, $GdAlO_3$. Opt Mater. 2017;63:207-212.
23. R. Klement, K. Drdlíková, M. Kachlík, D. Drdlík, D. Galusek, et al. Photoluminescence and optical properties of Eu^{3+}/Eu^{2+}-doped transparent Al_2O_3 ceramics. J Eur Ceram Soc. 2021;41:4896-4906.
24. G. Lee, N. Savage, B. Wagner, Y. Zhang, B. Jacobs, et al. Synthesis and luminescence properties of transparent nanocrystalline GdF_3: Tb glass-ceramic scintillator. J Lumin. 2014;147:363-366.
25. X. Liu, X. Qian, P. Zheng, X. Chen, Y. Feng, et al. Composition and structure design of three-layered composite phosphors for high color rendering chip-on-board light-emitting diode devices. J Adv Ceram. 2021;10:729-740.
26. J.A. Salem. Transparent armor ceramics as spacecraft windows. J Am Ceram Soc. 2013;96:281-289.
27. X. Ba, J. Li, Y. Zeng, Y. Pan, B. Jiang, et al. Transparent $Y_3Al_5O_{12}$ ceramics produced by an aqueous tape casting method. Ceram Int. 2013;39:4639-4643.
28. H. Yang, J. Zhang, D. Luo, H. Lin, D. Shen, et al. Novel transparent ceramics for solid-state lasers. High Power Laser Sci Eng. 2013;1:138-147.
29. B. Sun, L. Zhang, T. Zhou, C. Shao, L. Zhang, et al. Protected-annealing regulated defects to improve optical properties and luminescence performance of

Ce: YAG transparent ceramics for white LEDs. J Mater Chem C. 2019;7:4057-4065.

30. Q.-Q. Zhu, L.-Y. Hao, X. Xu, S. Agathopoulos, D.-W. Zheng, et al. A novel solid-state synthesis of long afterglow, Si–N co-doped, $Y_3Al_5O_{12}$: Ce^{3+} phosphor. J Lumin. 2016;172:270-274.
31. A. Koch, F. Peyrin, P. Heurtier, B. Ferrand, B. Chambaz, et al. X-ray camera for computed microtomography of biological samples with micrometer resolution using $Lu_3Al_5O_{12}$ and $Y_3Al_5O_{12}$ scintillators. Medical imaging 1999: Physics of medical imaging SPIE. 1999;3659:170-179.
32. A. Ikesue. Ce: YAG ceramic scintillator for electron beam detector. J Ceram Soc Jpn. 2000;108:1020-1023.
33. P.K. Sharma, R.K. Dutta, A.C. Pandey. Performance of YAG: Eu^{3+}, YAG: Tb^{3+} and BAM: Eu^{2+} plasma display nanophosphors. J Nanopart Res. 2012;14:1-9.
34. S. Li, Q. Zhu, X. Sun, J.-G. Li. Magical polyhedral twist via chemical unit co-substitution in $LaAlO_3$: Mn^{4+} to greatly enhance the zero phonon line for high-efficiency plant-growth LEDs. J Mater Chem C. 2021;9:7163-7173.
35. H.-K. Liu, L.-B. Liao, Y.-Y. Zhang, S.M. Aksenov, N. Liu, et al. Computational analysis of apatite-type compounds for band gap engineering: DFT calculations and structure prediction using tetrahedral substitution. Rare Metals. 2021;40:3694-3700.
36. F. Geng, Y. Matsushita, R. Ma, H. Xin, M. Tanaka, et al. Synthesis and properties of well-crystallized layered rare-earth hydroxide nitrates from homogeneous precipitation. Inorg Chem. 2009;48:6724-6730.
37. Q. Zhu, J.-G. Li, C. Zhi, R. Ma, T. Sasaki, et al. Nanometer-thin layered hydroxide platelets of $(Y_{0.95}Eu_{0.05})_2(OH)_5NO_3 \cdot x\ H_2O$: exfoliation-free synthesis, self-assembly, and the derivation of dense oriented oxide films of high transparency and greatly enhanced luminescence. J Mater Chem. 2011;21:6903-6908.
38. Q. Zhu, J.-G. Li, C. Zhi, X. Li, X. Sun, et al. Layered rare-earth hydroxides (LRHs) of $(Y_{1-x}Eu_x)_2(OH)_5NO_3 \cdot n\ H_2O$ (x= 0−1): structural variations by Eu^{3+}

doping, phase conversion to oxides, and the correlation of photoluminescence behaviors. Chem Mater. 2010;22:4204-4213.

39. J.A. Gadsden. Infrared Spectra of Minerals and Related Inorganic Compounds, Butterworth, Newton MA, 1975.
40. K. Nakamoto. Infrared Spectra of Inorganic and Coordination Compounds, John Wiley & Sons, New York, 1963.
41. Q. Zhu, S. Li, Q. Wang, Y. Qi, X. Li, et al. Grafting of terbium (III) complexes onto layered rare-earth hydroxide nanosheets to fabricate novel optical fiber temperature sensors. Nanoscale. 2019;11:2795-2804.
42. J. Li, F. Chen, W. Liu, W. Zhang, L. Wang, et al. Co-precipitation synthesis route to yttrium aluminum garnet (YAG) transparent ceramics. J Eur Ceram Soc. 2012;32:2971-2979.
43. L. Wen, X. Sun, Z. Xiu, S. Chen, C.-T. Tsai. Synthesis of nanocrystalline yttria powder and fabrication of transparent YAG ceramics. J Eur Ceram Soc. 2004;24:2681-2688.
44. T. Zhou, L. Zhang, S. Wei, L. Wang, H. Yang, et al. MgO assisted densification of highly transparent YAG ceramics and their microstructural evolution. J Eur Ceram Soc. 2018;38:687-693.
45. Q.-Q. Zhu, S. Li, Q. Yuan, H. Zhang, L. Wang. Transparent YAG: Ce ceramic with designed low light scattering for high-power blue LED and LD applications. J Eur Ceram Soc. 2021;41:735-740.
46. S. Li, Q. Zhu, X. Li, X. Sun, J.-G. Li. Near-infrared emitting microspheres of $LaAlO_3$: Mn^{4+}: defects engineering via Ge^{4+} doping for greatly enhanced luminescence and improved afterglow. J Alloys Compd. 2020;827:154365.
47. X. Li, W. Li, B. Hou, M. Jia, Y. Xu, et al. Investigation of enhanced far-red emitting phosphor $GdAlO_3$: Mn^{4+} by impurity doping for indoor plant growth LEDs. Physica B: Condensed Matter. 2020;581:411953.
48. R. Cao, W. Luo, Q. Xiong, A. Liang, S. Jiang, et al. Synthesis and luminescence properties of novel red phosphors $LiRGe_2O_6$: Mn^{4+} (R= Al or Ga). J Alloys Compd. 2015;648:937-941.

49. W. Lü, W. Lv, Q. Zhao, M. Jiao, B. Shao, et al. A novel efficient Mn^{4+} activated $Ca_{14}Al_{10}Zn_6O_{35}$ phosphor: application in red-emitting and white LEDs. Inorg Chem. 2014;53:11985-11990.
50. Y. Wang, C. Yu, Y. Zhou, E. Song, H. Ming, Q. Zhang. Mn^{4+} doped narrowband red phosphors with short fluorescence lifetime and high color stability for fast-response backlight display application. J Alloys Compd. 2021;855:157347.
51. X. Wu, Y. Yang, S. Gai, L. Liu, Z. Zhou, et al. Enhancing photoluminescence properties of Mn^{4+}-activated $Sr_{4-x}Ba_xAl_{14}O_{25}$ red phosphors for plant cultivation LEDs. J Am Ceram Soc. 2019;102:7386-7396.
52. Z. Pan, Y.-Y. Lu, F. Liu. Sunlight-activated long-persistent luminescence in the near-infrared from Cr^{3+}-doped zinc gallogermanates. Nat Mater. 2012;11:58-63.

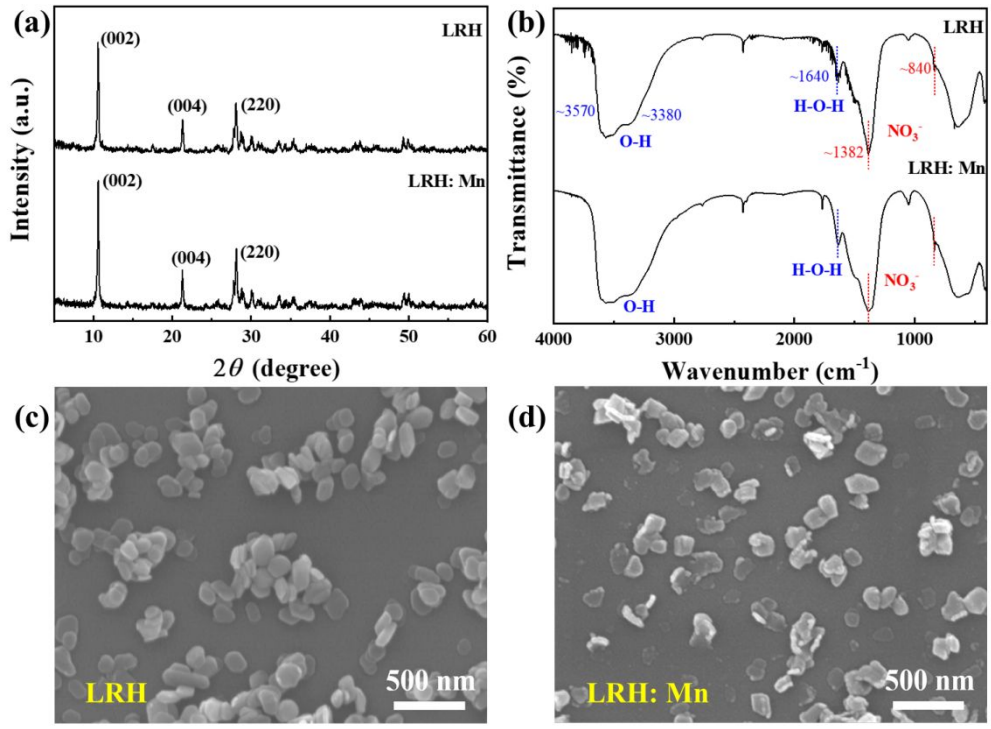

Figure 1. (a) XRD patterns, (b) FT-IR spectra, and (c, d) FE-SEM morphologies of LRH and LRH: Mn.

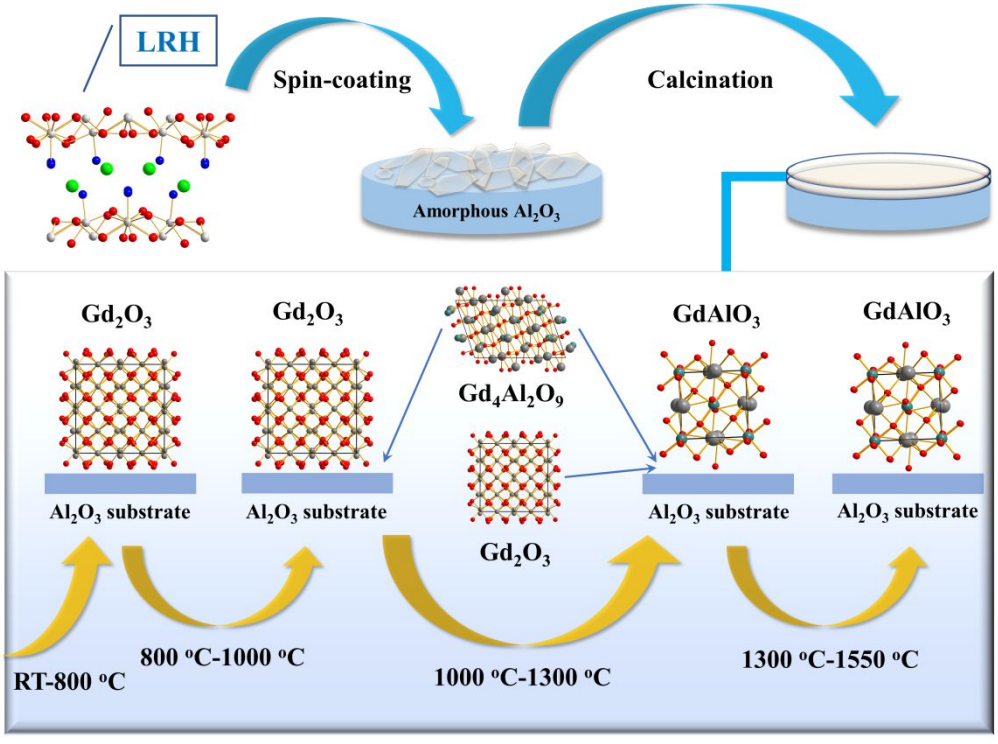

Figure 2. Schematic illustration of the phase evolution of ceramic film during the sintering process.

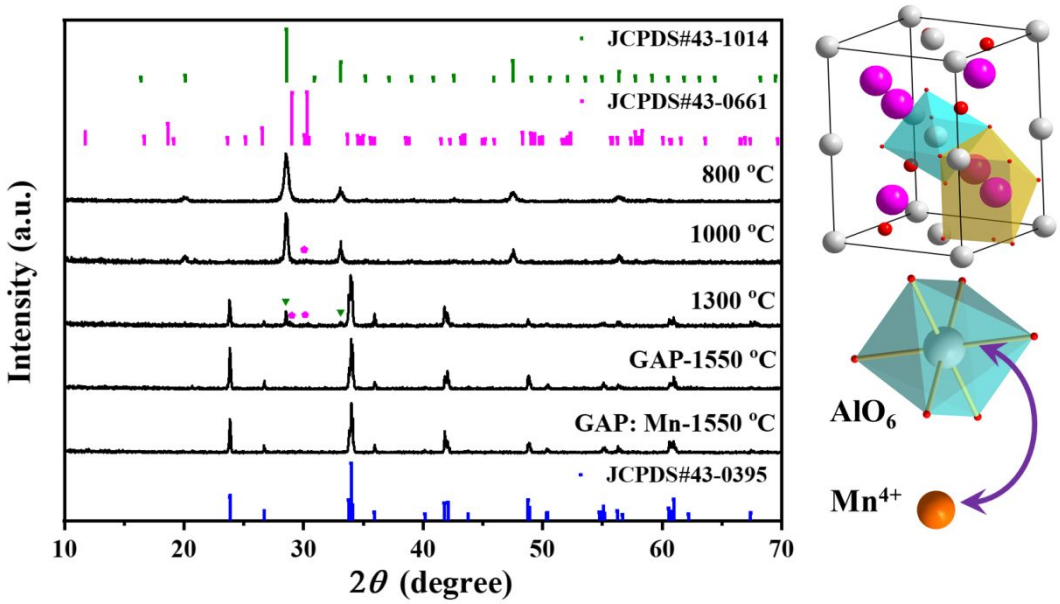

Figure 3. XRD patterns of the film calcined at different temperatures.

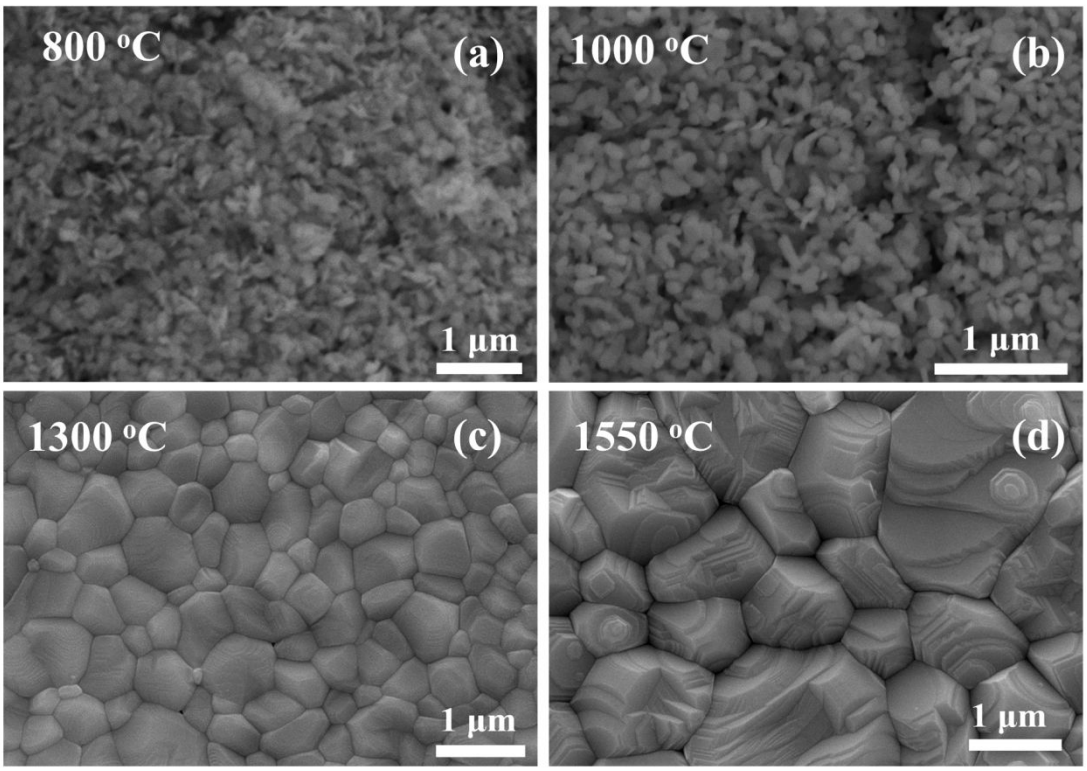

Figure 4. SEM morphologies of the film calcined at different temperatures.

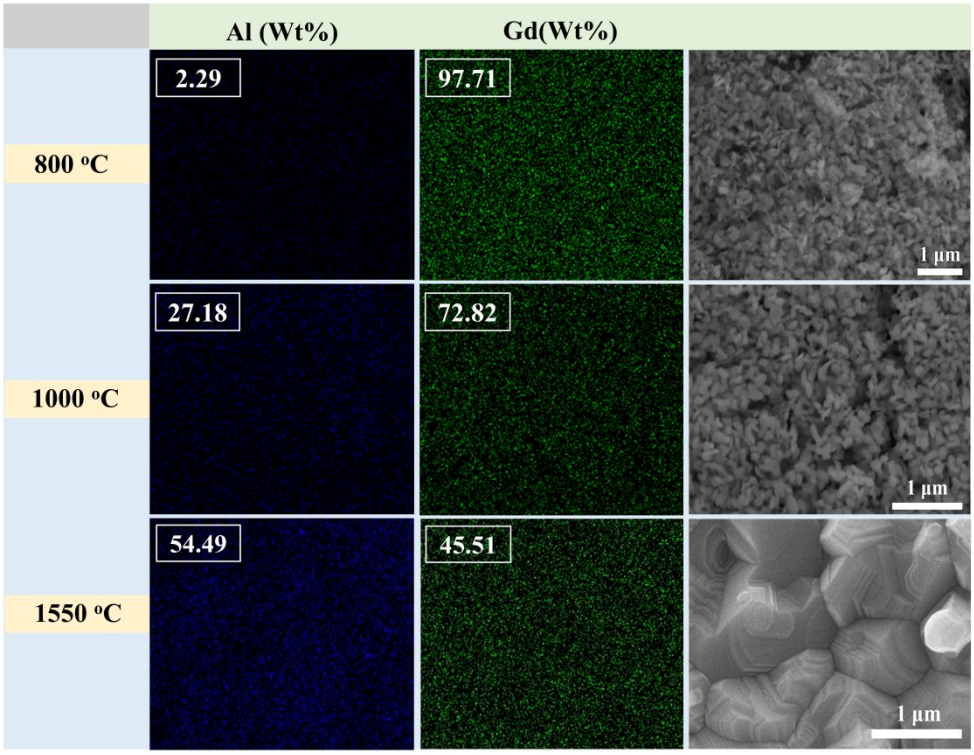

Figure 5. EDS elemental mapping analysis of the film calcined at different temperatures.

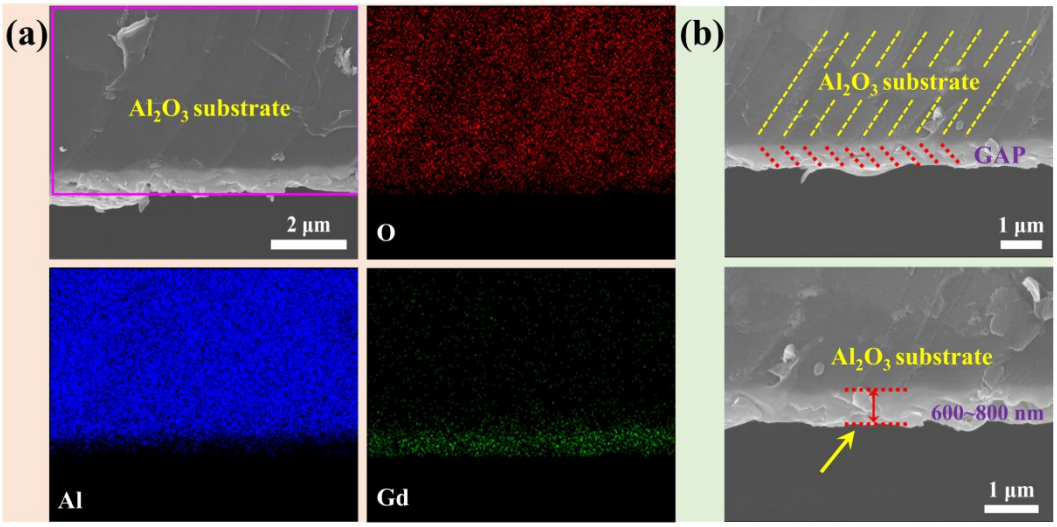

Figure 6. (a) EDS elemental mapping and (b) SEM morphologies of the cross section of GAP ceramic film.

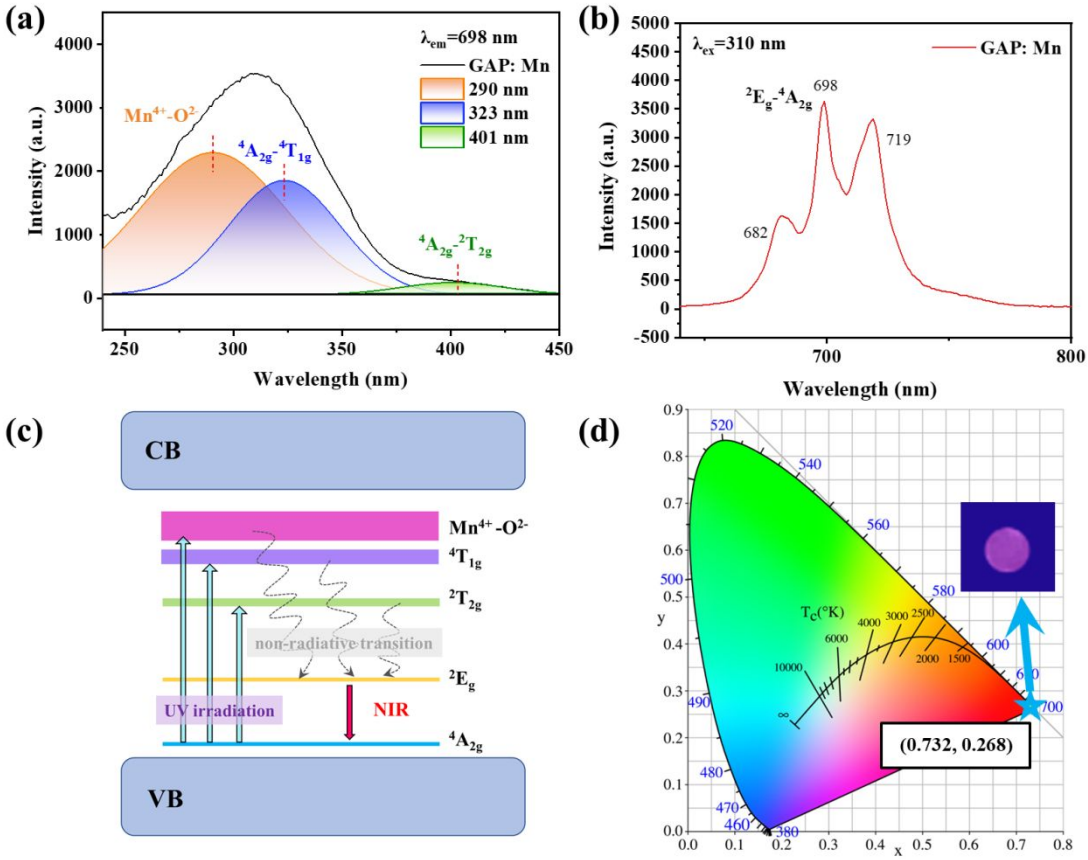

Figure 7. (a, b) PLE and PL spectra, (c) luminescence mechanism, and (d) CIE chromaticity diagram of GAP: Mn^{4+} ceramic film.

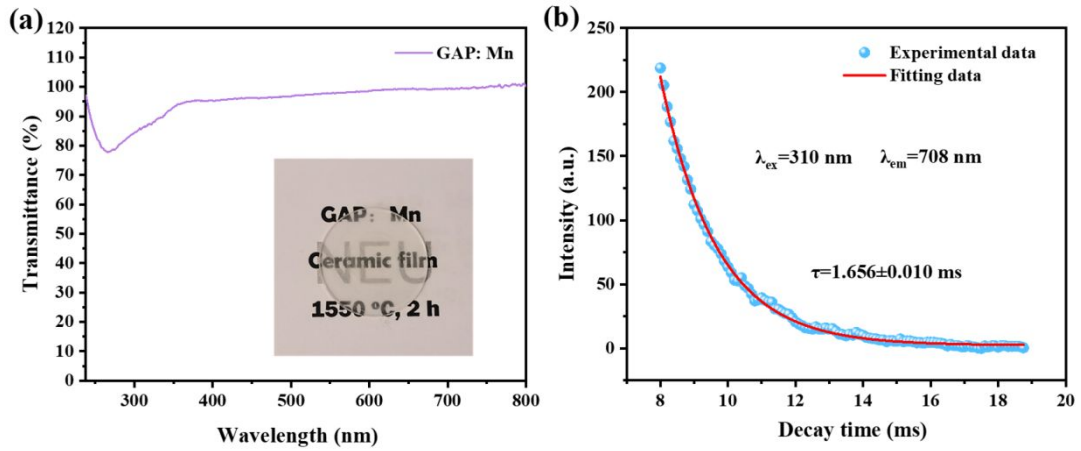

Figure 8. (a) Transmittance curve of GAP: Mn^{4+} ceramic film and (b) Fluorescence decay curve for the 708 nm emission of GAP: Mn^{4+} ceramic film.

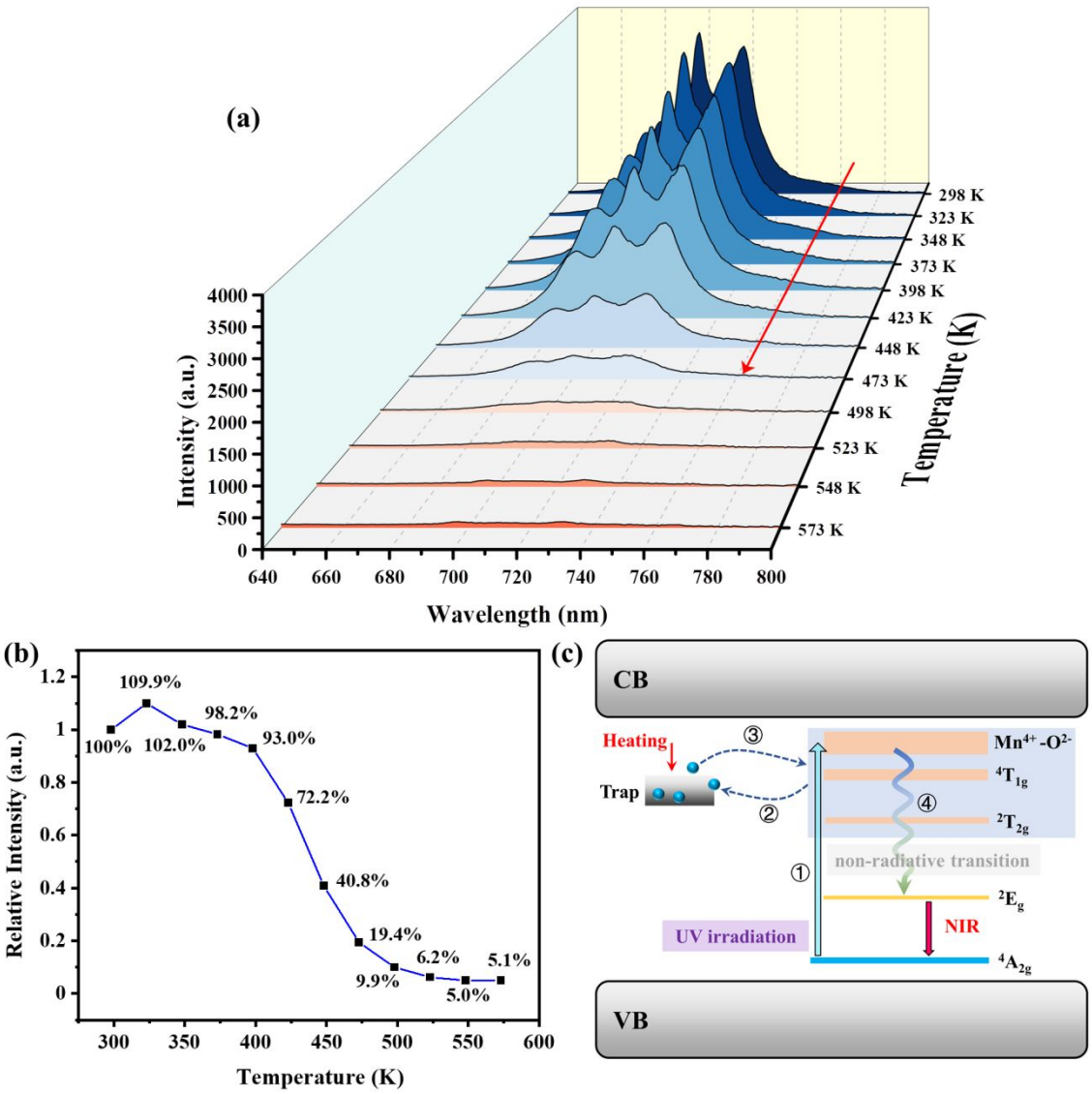

Figure 9. (a) Temperature-dependent PL spectra of GAP: Mn^{4+} ceramic film, (b) relative integral intensity of 698-nm emission, and (c) schematic diagram of fluorescence negative thermal quenching mechanism.

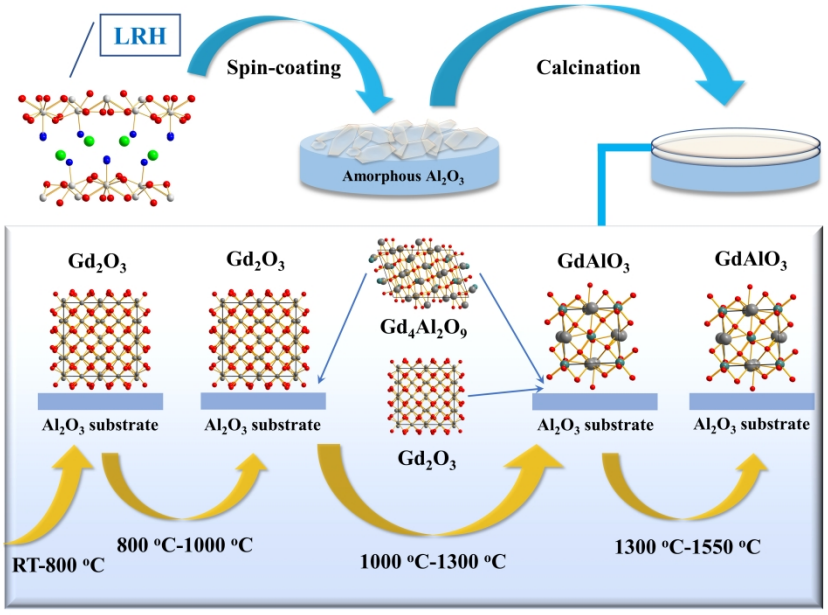

Graphic abstract

399x299mm (300 x 300 DPI)